

A laboratory model of marine snow: Preparation and characterization of porous fiber particles

Anna L. Dörgens,^{1,2} Soeren Ahmerkamp,² Jörg Müssig,¹ Roman Stocker,³ Marcel M. M. Kuypers,² Arzhang Khalili,^{*2,4} Kolja Kindler²

¹Department for Biomimetics, University of Applied Sciences Bremen, Bremen, Germany

²Department Biogeochemistry, Max Planck Institute for Marine Microbiology, Bremen, Germany

³Department of Civil and Environmental Engineering, Massachusetts Institute of Technology, Cambridge, Massachusetts

⁴Department of Earth and Space Sciences, Jacobs University Bremen, Bremen, Germany

Abstract

A method is described to prepare laboratory models of marine snow flocks using textile fibers to facilitate settling and mass transfer experiments under hydrodynamically well-defined conditions. A simple and effective roll-agglomeration process is introduced to fabricate macro-scale (up to centimeter-size) fiber particles, with predefined porosity, permeability, and excess density. Hydrodynamic similarity with natural marine snow aggregates was confirmed by measurements of porosity, permeability and settling velocity measurements. The assessment is completed by an analysis of the performance of the fabrication method. The fiber particles generated via this method can be used to advance our understanding of the hydrodynamics underlying settling dynamics and the associated mass transfer.

Marine snow flocks are aggregates of mostly biogenic origin which are >0.5 mm in size and have porosities ϕ often exceeding 95% (Turner 2002). Downward transport in the ocean is largely governed by marine snow settling. Due to their high concentration of organic matter, marine snow flocks constitute hotspots of microbial activity and metabolic turnover (Azam and Long 2001; Kiørboe et al. 2001). During their descent a complex exchange process between interstitial and ambient fluid occurs, affecting both local trophodynamics and large-scale mass transport (Kiørboe et al. 2002; Ploug and Passow 2007; De La Rocha and Passow 2007; Ploug et al. 2008; Kindler et al. 2010). To elucidate the fundamental hydrodynamics of mass transport by marine snow, simplified test aggregates are needed for laboratory experiments under well-defined hydrodynamic conditions.

Previously, spherical hydrogel particles (Kiørboe et al. 2002; Kindler et al. 2010) and fractal aggregates of coagulated microspheres (Johnson et al. 1996) have been used as models of marine snow to study the effects of microbial activity on mass transport. Fractal aggregates with inhomogeneous shapes and porosities lead to complex hydrodynamics and cumbersome experimental investigations. In case of hydrogel spheres, the very small pore size ($O(0.1-1\text{ nm})$) (Pernodet et al. 1997) inhibits microorganisms from colonising the internal structure, restricting microbial activity to the sphere surface.

Here, we report an inexpensive method to fabricate spherical porous fiber particles that mimic marine snow in a size range suitable for micro-scale, high-fidelity measurement techniques. We utilize synthetic textile fibers, easily available in a large range of finenesses, to form porous particles with predefined porosities ϕ , and permeabilities k . Three-dimensional, random assemblies of uniform fibers compose homogeneous porous structures, the permeability of which can be estimated by reference to random fiber webs (Koponen et al. 1998) as

$$\frac{k}{a_f^2} = 5.5 \left(e^{10.1(1-\phi)} - 1 \right)^{-1} \quad (1)$$

where a_f is the fiber radius. Solute distribution measurements in and around natural aggregates suggest that marine snow is nearly impermeable to flow (Li et al. 2003; Ploug and Passow 2007). Since Eq. 1 is solely a function of porosity and fiber radius, the permeability of the test aggregates can be tuned by the fineness of the fibers to investigate the influence of finite perfusion on mass exchange.

Hydrodynamic similarity requires reproducing the natural flow field and maintaining the relative importance of the different transport processes, namely diffusion and advection within and in the vicinity of the particle. The flow field is characterized by the ratio of inertial to viscous forces, expressed as the Reynolds number $Re = au/\nu$ where a is the sphere radius, u the velocity, and ν the kinematic viscosity. Natural settling in the ocean fall in the range $0.1 \leq Re \leq 10$

*Correspondence: akhalili@mpi-bremen.de

Table 1. Properties and process characteristics for model particles from polyester (PES), lyocell (LYO), and polyamide (PA). Permeability was measured at a porosity of $\phi = 0.95$, except for PA43 ($\phi = 0.9$). Stator depth h for stator type A was 12 mm for the finer, and 20 mm for the coarser PA fibers.

Material	T (tex)	a_f (μm)	ρ_f (kg m^{-3})	Stator type	a (mm)	Φ	ε	k/a_f^2
PES	0.22	7	1390	B	6.8(2)	0.972(8)	0.38(8)	12(3)
LYO	0.33	8	1540	B	7.4(5)	0.959(9)	0.44(9)	–
PES	0.44	10	1390	B	8.1(6)	0.967(7)	0.44(7)	–
PA	1.70	22	1140	A	8.6(2)	0.950(5)	0.40(7)	8(3)
PA	6.60	43	1140	A	13.2(5)	0.959(5)	0.36(4)	2(0)

depending on composition and size of the aggregates (Allredge and Gotschalk 1988; Ploug et al. 2008). The settling velocity of a solid sphere follows from the balance of buoyancy and drag forces, yielding (White 2005):

$$u_T^s = \sqrt{\frac{8 ag \Delta\rho}{3 C_D \rho}} \quad (2)$$

where g is the acceleration due to gravity, ρ the fluid density, C_D the drag coefficient, and $\Delta\rho$ the excess density

$$\Delta\rho = (1 - \phi)\rho_f + (\phi - 1)\rho \quad (3)$$

with ρ_f denoting the density of the fibers. The drag coefficient is in general a function of the Reynolds number and can be approximated by the empirical relation (White 2005)

$$C_D = \frac{12}{\text{Re}} + \frac{0.6}{1 + \sqrt{2\text{Re}}} + 0.4 \quad (4)$$

which is highly accurate in the range of Reynolds numbers of interest.

Particle permeability alters the front-aft pressure difference, consequently the drag, which can be accounted for by a correction to the solid sphere settling velocity. Assuming Darcy–Brinkmann flow in the interior, the settling velocity can be expressed as (Neale et al. 1973; Li et al. 2003)

$$u_T^p = \frac{2\xi^3 + 3(\xi - \tanh\xi)}{2\xi^2(\xi - \tanh\xi)} u_T^s \quad (5)$$

where $\xi = a/\sqrt{k}$ is the permeability factor. The impact of permeation on the flow field can be estimated by the ratio of the internal and incident flow velocities, referred to as the fluid collection efficiency (Wiesner 1993; Li et al. 2003)

$$\eta = \frac{9(\xi - \tanh\xi)}{2\xi^3 + 3(\xi - \tanh\xi)} \quad (6)$$

Strictly speaking, Eqs. 5 and 6 are restricted to creeping flow ($\text{Re} \ll 1$) when η is large. However, these relations are known to apply up to Reynolds number $O(1)$ (Li et al. 2003). Using Eqs. 5 and 6, the flow field in and around a porous

particle is completely defined by the set of a , ϕ , a_f , and $\Delta\rho$, i.e., by the particle size, the fiber type, and the fluid properties. Supplemented with the ratio of diffusion and viscous time scales given by the Schmidt number $\text{Sc} = \nu/D$ where D is the diffusion coefficient, the relative importance of diffusion and advection can be estimated as the Peclet number $\text{Pe} = \text{Re Sc}$. The target design is characterized by advection dominated transport at the sphere's surface ($\text{Pe} = au_T^p/D > O(1)$) and diffusion dominated transport inside the porous matrix ($\text{Pe}_i = a\eta u_T^p/D < O(1)$), with the average permeation velocity ηu_T^p .

Porous particle fabrication

Fibers

We used the synthetic fibers polyester (PES), lyocell (LYO), and polyamide (PA) to fabricate model aggregates. Synthetic fibers feature homogeneous circular cross sections. The fineness T is usually specified in weight per length 1 tex = 1 g km⁻¹. From this, the fiber radius is calculated as

$$a_f = \sqrt{\frac{1000T}{\pi\rho_f}} \quad (7)$$

where ρ_f the density of the fibers is taken from the manufacturer's data (Table 1). During manufacturing of fiber particles, relative humidity and temperature of the laboratory were held constant at 65% and 20°C, respectively. The resulting fiber particles were stored in the test liquid.

Roll-agglomeration

Spherical porous particles were generated from fibers using a modified roll-agglomeration process that was originally developed for the textile industry (Ay et al. 2005). Agglomerates were formed in air by adding loose fibers (approx. 300 mg) into a stationary chamber (stator) with a rotating top (rotor) in a process equivalent to fulling (Hildebrandt 2009). The rotor was driven electrically at 400 rpm. Stator and rotor were 6 cm in diameter and coated with abrasive paper with a grit of 60 to enhance fiber entrainment (compare Fig. 1). The stator was manually drawn close to the rotor while the fiber agglomerates built up until a spherical shape was achieved.

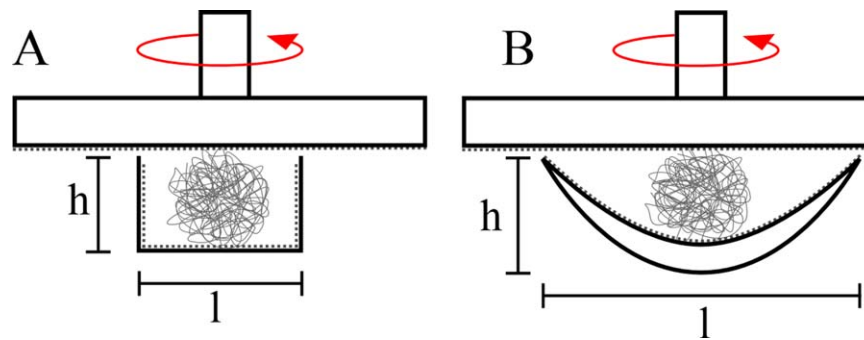


Fig. 1. (A) Roll-agglomeration setup with a concentric rotor design. The stator diameter is $l = 44$ mm and depth h is varied depending on the fiber radius (Table 1). (B) Roll-agglomeration setup with a eccentric rotor design. The axis of rotation is 21 mm off-centre. The stator diameter and depth are $l = 60$ mm and $h = 7.9$ mm.

In the present study, we seek to generate porous particles to cover different porosities and permeabilities. For this purpose, a wide range of fiber diameters were examined. Depending on the fineness of the fibers and the target size of the agglomerate two different rotor-stator arrangements were distinguished. The rotor can be positioned either concentrically (Fig. 1A) or eccentrically (Fig. 1B) above the stator. It was found that concentric rotation—similar to the design of Ay et al. (2005)—was suitable only for coarse fibers while eccentric rotation was more adequate for fine fibers. To avoid lateral escape of coarse fibers a rectangular stator was used instead of a concave one (Table 1). Once a particle was produced it was wetted slightly and underwent a second round of roll-agglomeration with an abrasive paper of larger grit (240).

Particle characterization

Eccentricity, sphericity and internal structure

To evaluate the performance and reproducibility of the porous particles, we analysed the eccentricity, equivalent radius, and microstructure. The shapes of the particles were quantified by images taken from three different angles against a dark background using a single lens reflex camera (D90, Nikon) and a 90 mm macro lens (focal ratio 2.8, Tamron) (Fig. 2A). The images were binarised and a pixel-connectivity algorithm was used to trace the boundary of the particle. Boundaries were approximated by ellipses, the principal axes (b , c) of which were averaged to deduce the mean eccentricity

$$\varepsilon = \sqrt{1 - \left(\frac{c}{b}\right)^2} \quad (8)$$

and the equivalent hydrodynamic radius $a = (b+c)/2$. Image processing was done in MATLAB (MathWorks).

Five sample series of nominally similar particles featured eccentricities of 0.4, equivalent to differences of the principal axes of up to 10%, which was considered satisfactory

conformance with the required spherical shape (Fig. 3). Particle radii varied between 6.5 mm and 14.0 mm and fell into the range of large-scale marine aggregates. The statistically significant trend of increasing sphere radius with increasing fiber radius ($c = 0.98$, $p < 0.05$, Pearson Correlation), can be associated with the larger flexural rigidity of thicker fibers. Eccentricity and equivalent radii were normally distributed and standard deviations were smaller than 1 mm, ensuring sufficient reproducibility of the process over the range of fiber radii considered.

The internal structure, i.e., the porous matrix, was characterized by casting representative agglomerates in OCT (Sakura, Tissue Tek) before sectioning them with an HM 505E microtome (Microm), with slice thicknesses comparable to fiber radii. Images of slices were binarised and the particle cross section was determined from the areal fiber density within the interrogation window (grey shaded Fig. 2). A two-dimensional closing algorithm was used to identify the cross sectional area and the boundary was approximated by least-square fitting to an ellipse (black lines in Fig. 2D,G).

Porosity was deduced from the thin slices as the ratio of fiber area to total cross sectional area. The values ranged from 0.92 to 0.96 (PES 7) and 0.93 to 0.95 (PA 43). Fibers appeared evenly distributed over the cross section with some loose fibers sticking out of the particles' boundary (Fig. 2). No predominant voids or fiber alignment in the circumferential direction were observed.

The internal structure was characterized by the azimuthally averaged structure function S , the square of the modulus of the spatial Fourier transform of the binarised thin section image. As apparent from Fig. 4, a single characteristic pore size cannot be identified from the wave number spectra (wave numbers k were scaled by fiber radii $2a_f$ to alleviate the comparison of different fineness). However, the two different power-law regions of the spectra can be associated with the spectral components of the pores and that of the fibers, respectively. The intersection of the two suggests effective pore sizes to exceed $7a_f$, corresponding to $O(10 \mu\text{m})$

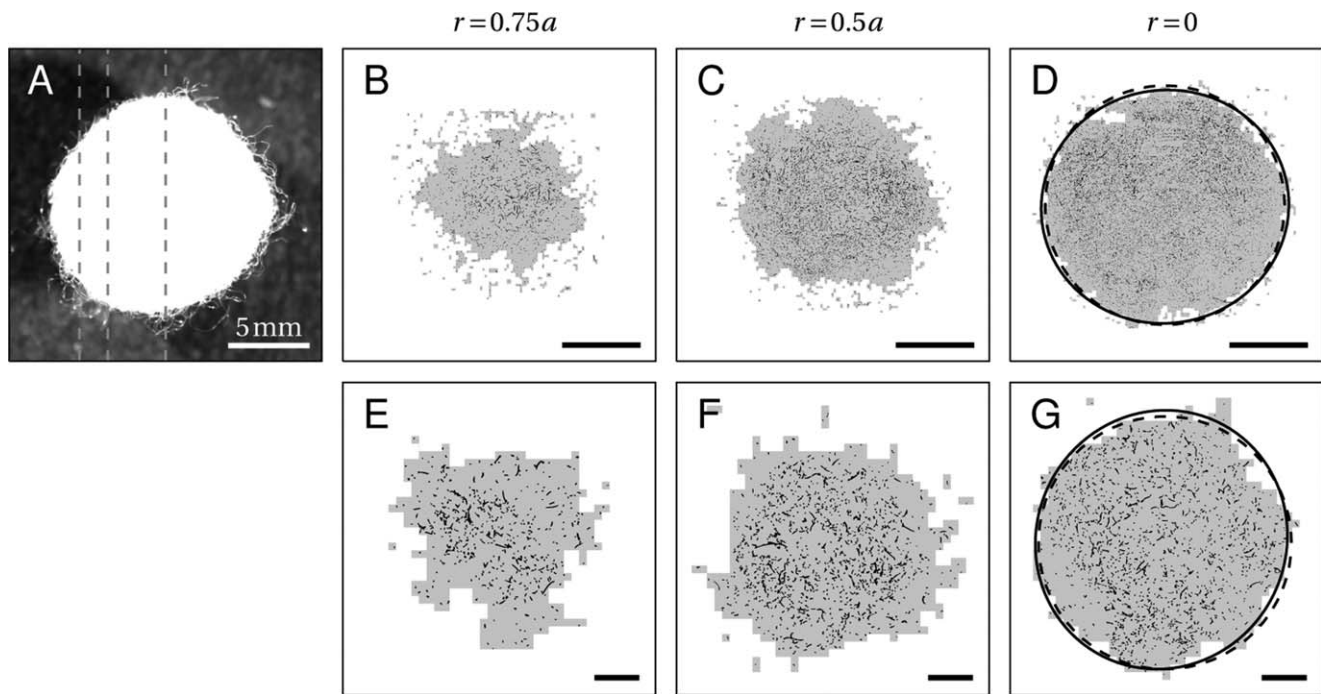


Fig. 2. Appearance and microstructure of porous particles. (A) Sample PES7 particle with dashed lines indicating the positions of the microtome samples, acquired at $r/a = 0.75, 0.5,$ and 0 . (B–G) Thin sections showing the fiber distribution (black) and the estimated cross-sectional area (grey shading) for PES7 (B–D, $a_{r=0} = 7.9$ mm) and PA43 (E–G, $a_{r=0} = 14.6$ mm). Scaling of all panels correspond to 5 mm. Dashed lines in D and G depict elliptical approximations of the particle boundary, whereas the solid line indicates the circle equivalent radius.

to $O(100 \mu\text{m})$ for the finest to coarsest fibers used. Note that the fiber diameter itself appeared as a slight spike at the normalised wave number $2ka_f = 1$ at the upper limit of the spectra.

Porosity was also determined from the volume fraction of fibers. Particle volumes were estimated as $V = 4/3(\pi a^3)$ and the (solid) fiber volume was calculated from fiber mass content and fiber density. Porosities varied between 0.93 and 0.97 with little fluctuation in individual batches (Fig. 2A), representing typical porosities for marine particles.

Permeability

The permeability was measured at porosities ranging from $\phi = 0.8$ to 0.95. A constant flow permeameter consisting of a cylindrical test chamber (30 mm, 40 mm, 50 mm and 70 mm in length and 25.8 mm in diameter d) and a syringe pump (LA-100, Landgraf Laborsysteme, Langenhagen, Germany) was used. Purified water (Milli-Q, Millipore) was chosen as test liquid (Dullien 1992).

The test chamber was fitted with an inlet and outlet of equal diameter and $5d$ in length, where the fiber sample was

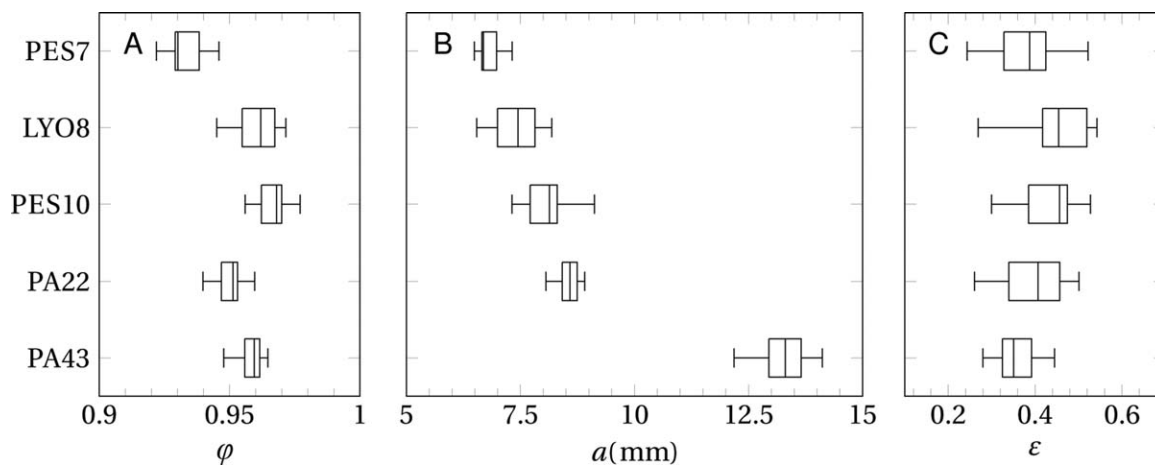


Fig. 3. Porosity (A), radius (B), and eccentricity (C) of model particles made of PES, LYO, and PA of various fiber radii ($N \geq 10$).

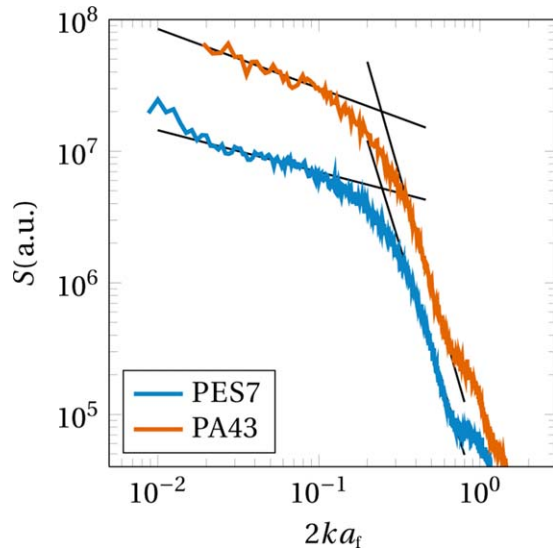


Fig. 4. Azimuthally averaged structure function S of the intensity image of the central thin section of particles PES7 and PA43 (Fig. 2D,G) vs. scaled wave number $2ka_f$. The intersection of the successive power-law trends $2ka_f = 0.27$ and 0.28 , respectively, indicate effective pore sizes larger than $7a_f$.

held in place by meshes with pore diameters of $700 \mu\text{m}$. Laminarity of the flow was ensured by pipe Reynolds numbers $Re_d = d\bar{u}/\nu$ well below $O(1000)$, where $\bar{u} = q\pi d^2/4$. Measuring the pressure loss $\nabla p = (p_{\text{in}} - p_{\text{out}})/L$ over the fiber length L of the sample, the permeability was calculated from Darcy’s law (Bear 1972)

$$-\frac{\mu}{k}\bar{u} = \nabla p \quad (9)$$

where μ is the dynamic viscosity of the test fluid.

Batches PES 7, PA 22, and PA 43 were examined, spanning a wide range of fiber radii (Fig. 5). Permeability increased with increasing porosity, which is consistent with greater voidage yielding larger pores, allowing fluid flow through the porous matrix. Permeabilities were compared to a model assuming 3-D randomly packed rods by Jackson and James (1986).

$$\frac{k}{a_f^2} = \frac{3}{20(1-\theta)} \left(\ln\left(\frac{1}{1-\theta}\right) - 0.931 \right). \quad (10)$$

Measured values for PES 7, PA 22, and PA 43 are in good agreement with models (Eqs. 1 and 10), with deviations increasing for finer fibers and larger porosities. The deviations from the models can be associated with varying, fineness-dependent mechanical properties of the fibers. The finer the fiber, the lesser its flexural stiffness, and the lower the volume fraction of fibers, the more susceptible the structure is to mechanical disruption and viscous forcing by the flow. Hence, internal re-organisation or re-alignment of fibers (Dullien 1992) might occur at large porosities as less

robust fiber webs are prone to forming fractures or macro channels which increase permeability. The maximum permeability in absence of macro channels can be estimated as the permeability of a structure with the flow normal to fibers in parallel alignment (Jackson and James 1986)

$$\frac{k}{a_f^2} = \frac{1}{4(1-\theta)} \left(\ln\left(\frac{1}{1-\theta}\right) + 1.5 + 2(1-\theta) - \frac{(1-\theta)^2}{2} \right) \quad (11)$$

which we include in Fig. 5 as the theoretical upper limit. We note that, in all cases, the permeability of the fiber particles was sufficiently small to ensure diffusion-dominated mass transfer between interstitial and ambient fluid.

Settling velocity

Settling experiments were performed in a 38 cm tall tank with a square base of $22.4 \times 22.4 \text{ cm}^2$. Two 150 W halogen lamps were used for illumination from the sides of the tank. The tank was filled to a depth of 36 cm with aqueous glycerol mixtures (Fauth technical glycerol), where the density and viscosity were used to control Re . Two different mixtures with $\rho = 1133 \text{ kg m}^{-3}$ and 1248 kg m^{-3} ($\nu = 6.0 \cdot 10^{-6} \text{ m}^2 \text{ s}^{-1}$ and $4.1 \cdot 10^{-4} \text{ m}^2 \text{ s}^{-1}$ (Cheng 2008)) were used (Table 1). To avoid residual flow, the tank was left to stand for 24 h prior to measurements. Particles were centrifuged at 3000 rpm in the same fluid as in the settling column for 5 min and released into the column via a cone to avoid lateral movements or rotations. The centrifugation itself did not alter the radius or other particle characteristics.

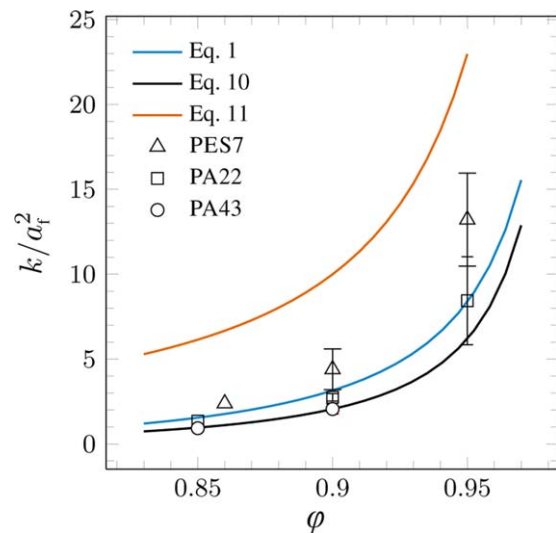


Fig. 5. Non-dimensional permeability k/a_f^2 as a function of porosity ϕ . Solid lines depict theoretical slopes for random fiber webs (Eq. 1), randomly packed fibers (Eq. 10), and flow normal to parallel fibers (Eq. 11). The latter defines the upper permeability limit for particles considered here.

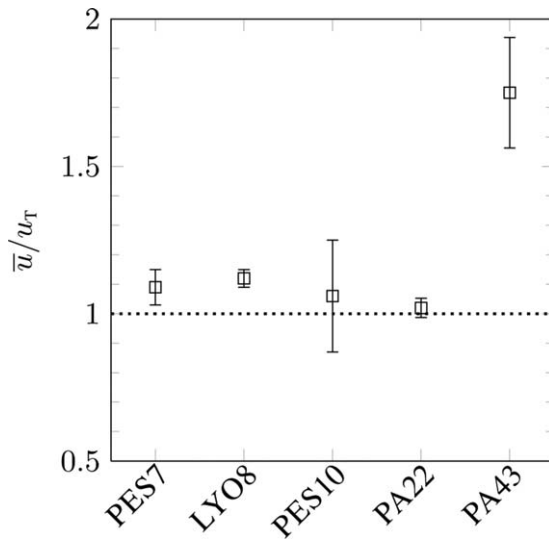


Fig. 6. Averaged, non-dimensional settling velocities of porous fiber particles at Reynolds numbers ranging from 0.6 (PES10) to 7.1 (PA22). Measured velocities were scaled by u_{τ} (Eq. 5) with error bars indicating standard deviations ($N = 10$).

To measure settling velocities, particles were imaged at 10 Hz using a pco.1600 camera (PCO) fitted with a F-S Nikkor zoom lens (Nikon, $f = 16$ to 88 mm, $f^{\#} = 3.5$ to 22) positioned 20 cm in front of the tank. The field of view was 10×5 cm² and the resolution was $270 \mu\text{m px}^{-1}$. The intensity image I was normalised $\tilde{I} = (I - I_{\text{ref}}) / I_{\text{ref}}$ by the undisturbed background I_{ref} . Subsequently, the largest connected white area was dissected by tracing the boundaries, where the centre of the particle was identified with the centre of gravity of an ellipse fitted to the boundary. Finally, the sinking velocity was calculated from the displacement using a five-point central difference scheme, corrected for wall effects (Clift et al. 2005), and averaged over ten experiments. Image processing was done in MATLAB.

Settling velocities for fiber particles were in the range of $3 \times 10^{-3} \text{ m s}^{-1}$ to $1 \times 10^{-2} \text{ m s}^{-1}$, falling into the same range as natural marine aggregates (Ploug et al. 2008). A comparison of the settling velocities with those estimated from Eq. 5 has been shown in Fig. 6. As can be seen, the measured values scatter slightly, approximately 10% above the theoretical ones. Only particles from PA 43 fibers had noticeably higher sinking velocities. Due to the relative strength of the PA 43 fibers, their surface appeared fuzzy (Figs. 2E–G, 3B). In addition, they contained fewer individual, but thicker and more rigid fibers resulting in larger inhomogeneity (Fig. 2G). This level of uncertainty can mainly be attributed to deviations in size and sphericity of individual aggregates.

Fluid collection efficiency

The fluid collection efficiency η was calculated from Eq. 6 using the experimentally obtained permeabilities. For a porosity of $\phi = 0.95$, η was found to range from $0.6(1) \times 10^{-4}$

to $2.0(7) \times 10^{-4}$ for PES 7 and PA 22 respectively. Fluid collection efficiencies were slightly lower for $\phi = 0.9$, spanning from $1.0(1) \times 10^{-4}$ for PA 43 to $0.2(6) \times 10^{-4}$ for PES 7 (Table 2). All fluid collection efficiencies were sufficiently small to neglect permeation effects on the settling behaviour and the flow field.

Discussion

Hydrodynamic similarity

The key demands of the target design (i.e., size, sphericity, porosity, and permeability) were all met by the resulting fiber particles. The fabrication procedure was found to be highly reproducible, providing good uniformity and sphericity of particles (diameters ranging from 6.8 mm to 13.2 mm). The particle geometry turned out to be largely limited by the quality or smoothness of the fiber surface. Coarser and more rigid fibers stuck to the abrasive paper hindering the control of particle sizes, thereby, limiting settling velocity predictions (Eq. 5).

For all fiber types, porosities of $\phi = 0.95$ were achieved. Maximum porosities were limited by the structural integrity and the associated interstitial homogeneity, both of which are related to the fiber fineness and bending stiffness. The best results were achieved for the finest fibers available, both in terms of maximising porosity and optimising homogeneity.

A key feature of the fiber particles is their very low permeability at effective pore sizes much larger than the characteristic size of microbial organisms. Porous particles composed of finest fibers have proven to provide low permeabilities which lie in the range of those of natural aggregates. The internal structure can readily be approximated as a homogeneous, random fiber web which is particularly simple to characterize and model. However, natural aggregates usually show heterogeneous structures, and as such they are bound to have physical properties that vary from point to point. For example, aggregates have also been found to be fractal-like when formed by sequential coagulation (Li and Logan 2001; Chellam and Wiesner, 1993). Diatom aggregates have been found to vary in porosity over time (Ploug et al. 2008). Porous particles also differ from natural aggregates in two other respects, being the surface shape and the interconnectivity of the voids. Due to these differences the flow around and through a porous particle might differ from the same for natural aggregates. While a porous particle might provide a constant resistance to a throughflow, natural aggregates provide varying resistance due to their heterogeneous structure. Consequently, the sinking behaviour, sinking speed and nutrition availability of natural aggregates and porous particles might deviate from each other. As far as porous particles with variable porosity and permeability are concerned the roll-agglomeration process can also be altered in a way to generate them (see ‘‘Comments and recommendations’’ section).

In contrast to agarose spheres, a common laboratory surrogate for marine snow (Kjørboe et al. 2002; Kindler et al.

Table 2. Hydrodynamic characteristics of porous fiber particles from polyester (PES), lyocell (LYO), and polyamide (PA). ξ and η were determined for a porosity of $\varphi = 0.95$, except for PA43 ($\varphi = 0.9$). Peclét numbers refer to $Sc = 700$ (representative for molecular diffusion).

Material	Re	ξ	$\eta \cdot 10^5$	Pe	Pe_i
PES7	0.6(1)	272(36)	0.6(1)	420	0.025
PA22	7.1(1)	157(46)	2.0(7)	4970	0.994
PA43	3.8(1)	215(15)	1.0(1)	2660	0.266

2010), not only the surface area but also the particle's whole porous matrix is available for colonisation, paving the way to respiration and turnover experiments.

Effective pore sizes of approximately $7a_f$ (for the finest fibers) and high porosities ensure that tortuosity effects are negligible (Bear 1972). Then, interstitial diffusive transport of all relevant substances can readily be approximated as free diffusion. The web-like microstructure will also facilitate intrusive measurements of dissolved gases (e.g., oxygen) inside the particles. Thus, traditional experimental methods such as oxygen-microsensor measurements frequently used on natural marine aggregates (Ploug et al. 2002; Ploug and Passow 2007; Ploug et al. 2008) can directly be conveyed to fiber particles.

Since the permeability measurements were performed on bundles of fibers and not on the generated porous particle themselves, some uncertainties may exist. Nonetheless, those uncertainties can be assumed to be insignificant, since the fluid collection efficiencies obtained from the permeability measurements were vanishingly small. Similar to natural marine snow, the porous particles were effectively impermeable to flow. Hence, mass transport or solute exchange between the interstitial and the ambient fluid can be assumed to be diffusion dominated.

Solute transport

As outlined above, the relative impact of diffusion on mass transfer is given by the Peclét number. Assuming $Sc = 700$, representative of dissolved gases, dissolved organic material, and amino acids (Kjørboe et al. 2001), natural bulk Peclét numbers are in the range of $Pe = 70$ to 7000 , i.e., external mass transport is advection dominated over the full range of Reynolds numbers. As can be seen from Table 2, the bulk Peclét numbers of the fiber particles fall within this natural range. However, residual permeation velocities inside the porous matrix might not be small compared to molecular diffusion ($Pe_i = O(1)$). Even if the permeation velocity ηu_T is negligible with respect to flow resistance, the condition of diffusion-dominated internal transport ($Pe_i = 1$) might be violated for coarser fiber particles. As a consequence, care must be taken to control interstitial and bulk Peclét numbers by adjusting the settling Reynolds number. Increasing sizes by a factor of 10 to improve spatial measurement resolution

requires a corresponding reduction of the settling velocity, for instance by reducing the excess density of the particles (by altering the viscosity of the test fluid).

Marine snow can be simulated in two ways. First, particles can be fabricated that directly simulate natural, large flocks, having the same size as the natural example settling in low viscosity solutions (i.e., seawater). Second, geometrically up-scaled particles can be examined in more viscous solutions (e.g., glycerol-water mixtures) to avoid excessive settling velocities, where appropriate Peclét numbers are obtained by considering thermal instead of molecular diffusion. The thermal diffusivity of concentrated glycerol-water mixtures is of order of $\kappa = O(10^{-7} \text{ m}^2 \text{ s}^{-1})$ (Lima et al. 2001) which facilitates size scalability over two orders of magnitude.

Comments and recommendations

The semi-manual process introduced here facilitates direct control of size and sphericity of the resulting fiber particles. Our roll-agglomeration approach is similar to a fully automated process available for the fabrication of (nearly) spherical porous fiber particles (Ay et al. 2005). However, greater flexibility in rotor-stator configurations and direct control of the porosity and permeability, given by our design, allow for generation of marine snow-like porous particles. Generally speaking, porous particles based on fibers of greater fineness were favourable with regard to processing and properties of the final particles. PA 7 particles seem most suitable to emulate marine snow for hydrodynamic measurements, while coarser fiber particles might be useful to investigate the impact of finite permeation on solute transfer.

The roll-agglomeration process can be altered to generate porous particles of variable porosities, similar to that of natural marine aggregates. This might be achieved by time-dependent alteration of the rotational speed of the rotor and the vertical rotor-stator distance. However, further experiments are required to explore the functionality and the similarity of such porous particles with real aggregates. Nevertheless, porous particles of uniform physical properties (e.g., porosity) and those with variable ones may serve different purposes. Uniform porous particles colonized with living organisms can be taken as a benchmark case to test the reliability of mathematical models for calculation of activities resulting from numerical solution of advection-reaction equations.

Upon demonstrating hydrodynamical similarity of the fiber particles with natural marine snow, the next step will be microbial colonisation. To make the particles nutritious several methods are possible depending on the fiber material selected. Protein and glycoproteins adhere to negatively charged glass fibers, whereas negatively charged organic matter would be more suitable for positively charged fibers. Alternatively, one may select fibers made of a specific organic matter such as cellulose, chitin, etc. which serve as substrate for bacteria.

References

- Allredge, A. L., and C. Gotschalk. 1988. In situ settling behaviour of marine snow. *Limnol. Oceanogr.* **33**: 339–351. doi:10.4319/lo.1988.33.3.0339
- Ay, P., C. Glaser, S. Hildebrandt, and S. Müller-Fehn. 2005. Method and device for producing spherical forms from fibre portions, WO 2005056172, 4 August 2005.
- Azam, F., and R. A. Long. 2001. Sea snow microorganisms. *Nature* **414**: 495–498. doi:10.1038/35107174
- Bear, J. 1972. Dynamics of fluids in porous media. Dover Publications.
- Chellam, S., and M. R. Wiesner. 1993. Fluid mechanics and fractal aggregates. *Water Res.* **27**: 1493–1496. doi:10.1016/0043-1354(93)90030-L
- Cheng, N.-S. 2008. Formula for the viscosity of a glycerol-water mixtures. *Ind. Eng. Chem. Res.* **47**: 3285–3288. doi:10.1021/ie071349z
- Clift, R., J. R. Grace, and M. E. Weber. 2005. Bubbles, drops, and particles. Dover Publications.
- De La Rocha, C., and U. Passow. 2007. Factors influencing the sinking of poc and the efficiency of the biological carbon pump. *Deep-Sea Res. II* **24**: 639–658. doi:10.1016/j.dsr2.2007.01.004
- Dullien, F. A. L. 1992. Porous media: Fluid transport and pore structure. Academic Press.
- Hildebrandt, S. 2009. Agglomeration von Fasermaterialien—Prozess- und anlagentechnische Untersuchungen der angepassten Faseragglomeration sowie deren Produktcharakterisierung zur Qualitätsbewertung (in German). Ph.D. thesis. Brandenburgische Technische Universität.
- Jackson, G. W., and D. F. James. 1986. The permeability of fibrous media. *Can. J. Chem. Eng.* **64**: 364–374. doi:10.1002/cjce.5450640302
- Johnson, C. P., L. Xiapyan, and B. E. Logan. 1996. Settling velocities of fractal aggregates. *Environ. Sci. Eng.* **30**: 1911–1918. doi:10.1021/es950604g
- Kindler, K., A. Khalili, and R. Stocker. 2010. Diffusion-driven retention of porous particles at density interfaces. *Proc. Natl. Acad. Sci. USA* **107**: 22163–22168. doi:10.1073/pnas.1012319108
- Kjørboe, T., H. Ploug, and U. H. Thygesen. 2001. Fluid motion and solute distribution around sinking aggregates. I. Small scale fluxes and heterogeneity of nutrients in the pelagic environment. *Mar. Ecol. Prog. Ser.* **211**: 1–13. doi:10.3354/meps211001
- Kjørboe, T., H.-P. Grossart, H. Ploug, and K. Tang. 2002. Mechanisms and rates of bacterial colonization of sinking aggregates. *Aquat. Microb. Ecol.* **68**: 3996–4006. doi:10.1128/AEM.68.8.3996-4006.2002
- Koponen, A., and others. 1998. Permeability of three-dimensional random fibre webs. *Phys. Rev. Lett.* **80**: 716–719. doi:10.1103/PhysRevLett.80.716
- Li, X.-Y., and B. E. Logan. 2001. Permeability of fractal aggregates. *Water Res.* **35**: 3373–3380. doi:10.1016/S0043-1354(01)00061-6
- Li, X.-Y., Y. Yuan, and H.-W. Wang. 2003. Hydrodynamics of biological aggregates of different sludge ages: An insight into the mass transport mechanisms of bioaggregates. *Environ. Sci. Technol.* **37**: 292–299. doi:10.1021/es020764+
- Lima, J. A. P., E. Marín, M. S. O. Massunaga, O. Correa, S. L. Cardoso, H. Vargas, and L. C. M. Miranda. 2001. Measurement of the thermal properties of liquid mixtures using a thermal wave interferometer. *Appl. Phys. B* **73**: 151–155. doi:10.1016/S0043-1354(01)00061-6
- Neale, G., N. Epstein, and W. Nader. 1973. Creeping flow relative to permeable spheres. *Chem. Eng. Sci.* **28**: 1865–1874. doi:10.1016/0009-2509(73)85070-5
- Pernodet, N., M. Maaloum, and B. Tinland. 1997. Pore size of agarose gels by atomic force microscopy. *Electrophoresis* **18**: 55–58. doi:10.1002/elps.1150180111
- Ploug, H., and U. Passow. 2007. Direct measurements of diffusivity within diatom aggregates containing transparent exopolymer particles. *Limnol. Oceanogr.* **52**: 1–6. doi:10.4319/lo.2007.52.1.0001
- Ploug, H., S. Hietanen, and J. Kuparinen. 2002. Diffusion and advection within and around sinking, porous diatom aggregates. *Limnol. Oceanogr.* **47**: 1129–1136. doi:10.4319/lo.2002.47.4.1129
- Ploug, H., M. H. Iversen, and G. Fischer. 2008. Ballast, sinking velocity, and apparent diffusivity within marine snow and zooplankton fecal pellets: Implications for substrate turnover by attached bacteria. *Limnol. Oceanogr.* **53**: 1878–1886. doi:10.4319/lo.2008.53.5.1878
- Turner, J. T. 2002. Zooplankton fecal pellets, marine snow and sinking phytoplankton blooms. *Aquat. Microb. Ecol.* **27**: 57–102. doi:10.3354/ame027057
- White, F. M. 2005. Viscous fluid flow, 3rd ed. McGraw-Hill.

Acknowledgments

The authors thank Peter Ay and Claudia Glaser from the Technical University of Cottbus for introducing us to roll-agglomeration techniques and processes. We also thank Axel Drieling and Tanja Sloomaker from FIBRE (Faserinstitut Bremen e.V.) for a helpful discussion about fiber measurement techniques. The authors are indebted to Helle Ploug from the University of Stockholm for valuable comments and discussion. The supply of fiber samples by Cetex-Rheinfaser (Ganderkesee, Germany) and Dorix Chemiefaserwerk (Selbitz, Germany) is also gratefully acknowledged. Roman Stocker acknowledges support from NSF through grant OCE_0744641_CAREER and CBET_1066566. The authors are grateful to the Max Planck Society for the financial support of this study.

Submitted 13 February 2015

Revised 14 July 2015

Accepted 17 July 2015

Associate editor: Prof. Gordon Taylor